IOP Publishing Plasma Sources Science and Technology
Plasma Sources Sci. Technol. **31** (2022) 095001 (15pp) https://doi.org/10.1088/1361-6595/ac8449

Experimental and simulation study of a capacitively coupled radiofrequency plasma with a structured electrode

Ján Ďurian[1,*], Peter Hartmann[2], Štefan Matejčík[1], Andrew R Gibson[3,4] and Zoltán Donkó[2]

[1] Department of Experimental Physics, Faculty of Mathematics, Physics and Informatics, Comenius University in Bratislava, Mlynská Dolina F2, 84248 Bratislava, Slovakia
[2] Institute for Solid State Physics and Optics, Wigner Research Centre for Physics, 1121 Budapest, Konkoly Thege Miklós Str. 29-33, Hungary
[3] Institute of Electrical Engineering and Plasma Technology, Ruhr-Universität Bochum, Universitätsstraße 150, 44801 Bochum, Germany
[4] Research Group for Biomedical Plasma Technology, Ruhr-Universität Bochum, Universitätsstraße 150, 44801 Bochum, Germany

E-mail: durian5@uniba.sk

Received 4 May 2022, revised 6 July 2022
Accepted for publication 26 July 2022
Published 30 August 2022

Abstract

A low-pressure capacitively coupled radiofrequency (RF) helium discharge with a structured electrode is investigated experimentally and via kinetic simulations. In the experiment, phase resolved optical emission spectroscopy provides information about the excitation dynamics by high energy electrons, with high spatial and nanosecond temporal resolution within the RF (13.56 MHz) period. The numerical studies are based on a newly developed 2d3v particle-in-cell/Monte Carlo collisions code carried out on graphics processing units. The two approaches give consistent results for the penetration of the plasma into the trench situated in one of the electrodes and the particular electron dynamics resulting from the presence of the structured electrode. In addition, the fluxes of He^+ ions and vacuum ultraviolet photons incident on the different surfaces in and around the trench structure are studied. These are discussed with respect to the homogeneous treatment of complex structures, relevant for advanced surface modification and disinfection processes.

Keywords: structured electrode, PIC/MCC, radio-frequency, capacitively coupled plasma, VUV photon tracing, surface treatment

(Some figures may appear in colour only in the online journal)

1. Introduction

Low pressure plasma sources are widely used for the treatment of surfaces. Prominent examples include the modification of surfaces (cleaning, surface energy modifications), plasma etching of materials or the deposition of coatings [1, 2]. There is also strong interest in the use of such plasma sources for the disinfection or sterilisation of temperature sensitive materials [3–5]. The active species that drive these processes are ions, radicals and ultraviolet/vacuum ultraviolet (UV/VUV) photons emitted by excited species. In most applications, a homogeneous treatment of the whole surface exposed to the plasma is desired, which implies that the fluxes of the relevant components should be equal at all locations to be treated. The homogeneity of the plasma, and the fluxes of active components to surfaces is strongly influenced by the plasma reactor design, including the mode of plasma formation and the overall dimensions. In addition, the shape of the object

* Author to whom any correspondence should be addressed.

to be treated is particularly important due to the nature of the plasma-surface interaction. In this context, achieving homogeneous treatments of flat surfaces, is straightforward compared to surfaces with complex structures.

The treatment of complex surface structures is particularly important in the context of a number of emerging applications of plasma technology. For example, the coating or sterilisation of medical devices [2, 5]. In the case of surface sterilisation, for example, the minimum process time will be determined by the time required to inactivate microorganisms on all surfaces of a given object. This, in turn, is dependent on the homogeneity of the fluxes of active components to these surfaces. The particular mechanism of action leading to disinfection or sterilisation can, in principle, be related to a variety of plasma-produced species such as reactive neutrals, high energy ions or UV photons. The precise mechanism in a given plasma source will depend on the particular gas mixture and overall operating conditions. Whether or not these active components can reach all surfaces of an object to be treated will depend on the dimensions of the relevant features, and their relation to the plasma sheath length. While these dynamics are highly application relevant, a detailed understanding of the fundamental plasma properties, and associated fluxes of relevant species to surfaces, during plasma interactions with complex surfaces is still to be developed. An active combination of experimental and computational approaches offers an ideal solution to develop this understanding.

Radio-frequency plasmas are a common choice for many of the discussed applications. These plasmas exhibit complex dynamics on the nanosecond time scale as a consequence of the fact that electrons can follow the rapid spatio-temporal variation of the electric field. These dynamics are key to determining the overall properties of these sources through their role in determining the time and space resolved electron energy distribution function (EEDF). This, in turn, determines the time and space resolved production of active components that drive application outcomes. Phase resolved optical emission spectroscopy (PROES) [6–10] is a powerful experimental method that can aid obtaining information about these dynamics. PROES is conventionally conducted on a selected spectral line of which the upper level has a high excitation threshold. This ensures that the dynamics of high-energy electrons, being also responsible for ionisation, is captured. In addition, PROES can be used to partially validate the electron dynamics predicted by numerical simulations which, in turn, can be used to give insight into fundamental processes such as electron heating, and to understand the fluxes of particles to surfaces.

The aim of this work is to generate a detailed understanding of the plasma properties and particle fluxes to surfaces in a well-defined, but non-planar geometry that can be effectively studied through a combination of experiment and simulation. For this purpose, a capacitively coupled radio-frequency plasma operated in He is used. The grounded electrode in the system contains a trench structure that is well suited for study via PROES and a newly-developed 2d3v particle in cell/Monte Carlo collisions (PIC/MCC) code. Similar electrode geometries have been studied previously in other contexts, for example, as a mechanism to control plasma uniformity in processing applications [11–15]. Using this system, the main purposes of the work are: (i) from the fundamental point of view, to understand the operation of the discharge with a structured electrode. Here, the focus is on the analysis of the spatio-temporal distribution of the excitation and ionization processes and the penetration of the plasma into the trench of the electrode; (ii) related to applications, determination of the energy distributions of the positive ions as well as the flux of these ions and VUV photons to the different surface elements of the structured electrode using the simulation, having in mind that these species play the key role in applications involving the treatment of complex surface structures, such as sterilisation.

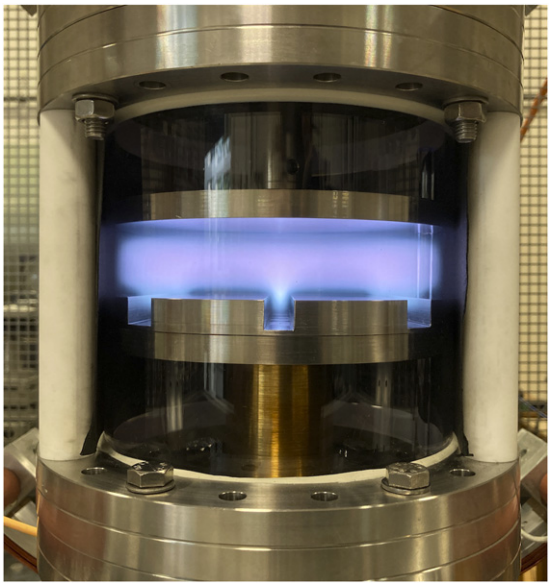

Figure 1. Photograph of the discharge with the structured (grounded) electrode at the bottom. The gas is helium, at a pressure of 60 Pa.

The paper is structured as follows: in section 2, we describe the experimental setup and the diagnostics systems. In section 3.1, the numerical methods: the 2d3v PIC/MCC simulation method and the approach for tracing the VUV He resonance photons are introduced. The experimental and simulation results are presented in section 4, while conclusions are given in section 5.

2. Experimental system and methods

A sketch of the experimental setup, which has already been described in detail in [16], is shown in figure 2. Our studies are conducted with a geometrically symmetric CCP source ('Budapest v.3 Cell') equipped with flat disk electrodes, made of type 304 stainless steel with a diameter of 14 cm. For the present experiments, one of the electrodes is modified: three trenches, each having a width and a depth of 1 cm have been machined into the bottom (grounded) electrode. One of the trenches in located along the diameter of the disk, and the others are situated parallel to this 'main' trench, 5 cm

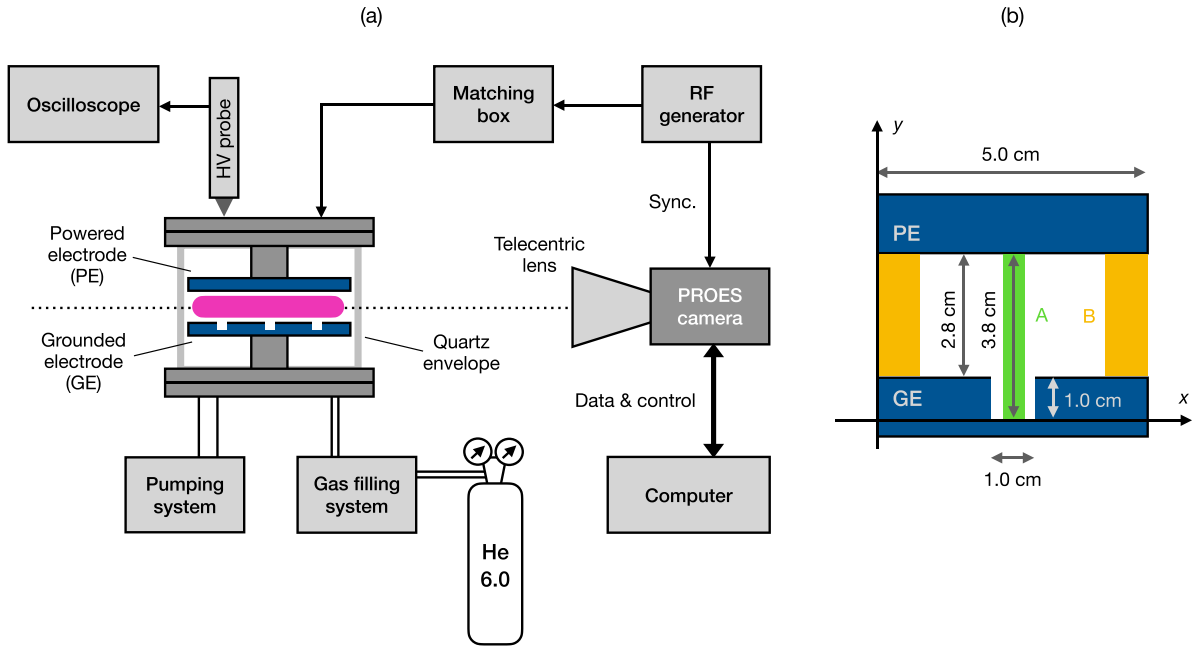

Figure 2. Scheme of experimental system (a) and the enlarged view of the central part of the electrode system (b), which represents the computational domain: 0 cm $\leqslant x \leqslant$ 5 cm, 0 cm $\leqslant y \leqslant$ 3.8 cm. In the simulations, periodic boundary conditions are applied at the left and right sides of this domain. PE: powered electrode, GE: grounded electrode, the green ('A') and yellow ('B') colors mark domains for which spatio-temporal distributions of the excitation rate will be presented.

apart in both directions, as shown in the photograph of the plasma source in figure 1. This configuration approximates the periodicity of trenches assumed in the simulations (see later). We note, that in the absence of this modification the cell is highly symmetric, the DC self-bias voltage is in the order of 1% of the applied RF voltage. Therefore, the DC bias voltage values measured with the modified electrode can be considered to originate exclusively from the geometric asymmetry caused by the trenches.

The sketch of the experimental setup is shown in figure 2(a), while more details of the electrode geometry are shown in figure 2(b). The electrodes are enclosed by a quartz cylinder and the cell is evacuated via a gate valve by a turbomolecular and a rotary pump. The background pressure of the system is approximately 10^{-5} Pa. The experiments are performed in He gas, with a flow of ∼1.4 sccm set by a mass flow controller. A needle valve allows fine control of the gas pressure in the chamber, measured by capacitive gauges (Pfeiffer Vacuum CMR264 and MKS Baratron 631A). The upper electrode of the cell is driven by a RF generator via a matching box (Tokyo Hy-Power RF-150 and MB-300), while the lower electrode is grounded. The peak-to-peak value of the applied voltage is measured by a HP 54602B oscilloscope equipped with a high voltage probe (Agilent 10076B). The discharge is driven at a frequency of $f_0 = 13.56$ MHz, the pressure is scanned between $p = 40$ Pa and 140 Pa, while the peak-to-peak driving voltage is fixed at $\phi_{pp} = 340$ V.

The main diagnostic tool of the setup is a fast-gateable ICCD camera (Stanford 4 Quick-E) equipped with a telecentric lens (Edmund Optics TitanTL 0.191X). The optical axis is aligned with the 'main' trench of the bottom electrode of the cell. During the experiments, the emission is monitored from the He 3s state at a wavelength of 706 nm using an interference filter with a central wavelength of 710 nm and a spectral full width at half maximum of 10 nm. No other emission lines within this domain influence the measurements. The trigger signal of the camera is synchronized with the RF generator and the gate time of the camera is set at 2 ns. The spatial resolution is determined by the number of pixels in the camera sensor: the 780 × 580 pixels result in a resolution of approximately 88 μm.

The theoretical consideration behind PROES is based on population dynamics: the method operates based on the time-dependent measurement of the population density of a specifically chosen excited rare gas state, as described in [9]. The basic concept of the measurement is that the spatio-temporal electron impact excitation rate from the ground state into the observed level, $E_{0,i}(x,t)$, can be evaluated from the measured spatio-temporal emission. In order to perform a PROES measurement on a CCP based on the analysis presented in [9], (i) the relevant optical transition rates need to be known, (ii) the population of the excited states due to cascades, excitation from metastable levels and quenching need to be negligibly low, (iii) high enough intensity of the measured emission line is necessary and superposition with other lines within the spectral resolution of the spectrometer or the interference filter has to be avoided, and finally, (iv) the lifetime of the relevant excited state has to be short enough to temporally resolve the RF period (the period being ∼74 ns here). The 706.52 nm transition with the upper level He 3s having a lifetime of 35.9 ns satisfies these criteria [17]. We note that quenching effects are not included in our data analysis procedure.

3. Numerical methods

Below, we outline the basics of the main computational approach, the PIC/MCC simulation method (in section 3.1) and the treatment of the resonant radiation transport in the plasma (in section 3.2).

3.1. 2D PIC/MCC simulations

Present numerical studies are based on the PIC/MCC simulation approach, which is widely adopted in modelling of capacitively coupled radio-frequency discharges, see, e.g. [18–27]. This approach is based on tracking individual charged particles in space and time whilst taking into account their self-consistent space charge density computed via a computational grid spanning across the simulation domain, as well as their interaction (collisions) with the neutral background gas and with the surfaces of the electrodes. As typical laboratory plasmas contain large amounts of charged particles it is impossible to track them all individually. To alleviate this issue, instead of tracking individual particles, the PIC/MCC method tracks groups of such particles called 'superparticles' [19]. Even with this approach implemented, PIC/MCC models remain computationally intensive, especially if more than one spatial dimension needs to be resolved, such as in our case where a structured electrode is present in the system. With the advance of general purpose GPU (GPGPU) computing, a number of GPU-accelerated PIC/MCC implementations have been developed, further dealing with the issues of the computational demands that the PIC/MCC models inherently bring [28–33].

In the PIC/MCC scheme, both space and time are discretized, defining the spatial and temporal resolution of the computations. In this study, a 2D mesh with uniform resolution Δx and Δy, respectively, in the x and y directions was used. The computations yield the plasma characteristics at the points of this grid. Discretization in time allows the numerical solution of the equations of motion of the charged particles. The plasma characteristics (electron density, Debye length, collision frequencies) impose a number of conditions on the spatial and temporal resolutions, for the stability and the accuracy of the calculations (see, e.g. [34, 35]).

The computational scheme consists of several components. As already mentioned, the PIC/MCC method tracks the movement of individual superparticles in an electric field defined by the electrode potentials and the spatial distribution of the space charge within the volume. To compute this electric field, the space charge needs to be assigned (via interpolation) to the points of the computational grid and the Poisson equation,

$$\Delta\phi(\mathbf{r}) = \frac{\rho(\mathbf{r})}{\varepsilon_0}, \tag{1}$$

has to be solved. From the potential, the electric field is obtained as

$$\mathbf{E}(\mathbf{r}) = -\nabla\phi(\mathbf{r}), \tag{2}$$

which allows advancing the particles in space, according to their equations of motion:

$$\ddot{\mathbf{r}} = \dot{\mathbf{v}} = \frac{q}{m}\mathbf{E}(\mathbf{r}). \tag{3}$$

Following these steps, the probability of collision has to be computed for each particle and a collision event needs to be simulated if certain conditions are met. Collisions are handled with a stochastic (Monte Carlo) approach, the details of which are given in, e.g., [36]. Particles that have reached the boundaries have to be removed from the simulation. These steps are conducted in the PIC/MCC scheme in a cyclic manner, typically several thousand times within an RF cycle.

A newly developed Cartesian 2d3v GPU-accelerated PIC/MCC code is used to model the discharge. The host code is written in C++ and utilizes OpenMP for CPU-side computations while the device code running on the GPUs is based on the CUDA technology. The numerical methods used in the code were optimized for parallel computing as follows: (i) the field solver uses a parallelized version of the iterative successive over-relaxation (SOR) algorithm for solving the Poisson equation, (ii) the particle mover uses the Leapfrog integration scheme, and was massively parallelized on a 'one particle per thread' basis with thread synchronization based on atomic operations.

The execution of the code starts with loading all relevant simulation input parameters and seeding the initial simulation state by pre-computing electrode potentials and randomly (and uniformly) distributing particles of all present species across the simulation domain. Subsequently, the main simulation follows, which is split into the (i) convergence and (ii) diagnostics stages. During the convergence stage, only the particle numbers are monitored. Diagnostic data are not collected until the simulation converges to a periodic steady state (determined by the particle counts remaining at an overall constant level), and the diagnostic stage of the simulation begins. The code requires simulation of 2000–3000 RF cycles to reach convergence, with the exact number depending on the gas pressure. Diagnostic data are collected during the subsequent 1000 RF cycles.

Concerning the implementation of the steps of the PIC/MCC scheme [36]: (i) the field solver (parallelized SOR) is performed on the GPU. Once per several iterations residuals are computed and copied to the CPU for a convergence check. The interval at which this happens is automatically and dynamically determined during runtime as a performance optimization to minimize the amount of (slow) data transfers between the CPU and GPU. (ii) The particle mover is performed on the GPU, and is massively parallelized by having every thread executed on the GPU perform all necessary computations on its own assigned particle. This design is discussed in detail for one-dimensional PIC/MCC codes in [28]; similar principles apply in two-dimensional PIC/MCC models. (iii) Monte Carlo collisions are performed on the GPU as well, and the algorithm itself is integrated into the particle mover as a performance optimization to minimize the number of kernel calls to the

GPU. (iv) Particle removal is done on the CPU after evaluating each RF cycle. All particle data are copied to the CPU memory for sorting and filtering out of all particles that have become inactive during the evaluation of the RF cycle (particles that got absorbed at the electrode). The filtered data are then copied back to the GPU, and the simulation resumes.

The dimensions of the simulation domain defined by the model are 5 cm (laterally) by 3.8 cm (vertically) as shown in figure 2(b). Periodic boundary conditions are applied at the left and right sides of this domain. This is reflected in the boundary conditions for the Poisson equation, as well as on the particles that are being moved to the opposite side of the simulation domain upon crossing the periodic boundary. The resolution of the computational grid is 256 × 192 points, which results in near-square grid cells given the dimensions of the simulation domain.

In the collision model, electron-neutral and ion-neutral collisions are taken into account. For the electron-neutral collisions a cross-section set known as 'Biagi v8.92' [37] is used. This set consists of 51 collision types in total (elastic collision, 49 excitation states and ionization). For the ions, only elastic collisions with neutral atoms are considered, consisting of an isotropic and a backwards scattering component, as proposed in [38]. The cross-section set for these two collision types is taken from [39]. In the collision model isotropic elastic scattering is assumed and in accordance with this we use the elastic momentum transfer cross section.

Secondary electron emission and electron reflection effects are modelled at the electrode surfaces. Coefficients of $\gamma = 0.3$ and $\rho_e = 0.7$ are used for these two phenomena respectively, which is a good estimate for the combination of the background helium gas and the stainless steel material used for the electrodes in the experimental setup [40–42].

The discharge is excited by a harmonic waveform, $\phi(t) = 0.5\phi_{pp}\cos(2\pi ft)$, with $\phi_{pp} = 340$ V. The DC self-bias voltage, η, that develops in the discharge due to the geometrical asymmetry, and modifies the discharge voltage to be $\phi_d(t) = \phi(t) + \eta$, is determined in an iterative way. The simulations are initialized with a zero value of this parameter and after a certain number (N_b) of RF cycles the flux balance between the positive ions and electrons reaching the powered electrode is evaluated. Depending on this balance η is changed by a small value and this value is used in the forthcoming N_b RF cycles. This procedure is repeated until a balance of the fluxes is reached (with some fluctuations due to the finite number of particles in the simulations). The simulations are executed for five different pressures: 40 Pa, 60 Pa, 80 Pa, 100 Pa and 140 Pa. The gas temperature was assumed to be 300 K.

The simulations comprise about 5 to 9 million superparticles per species, which results in about an average of 100–180 superparticles per species per grid cell. The calculations have been executed using Quadro RTX 4000 GPU cards, with the above number of superparticles in the converged state. The simulation of 1000 RF cycles during which data have been accumulated for the final results took about 15 h.

3.2. Tracing of resonant VUV photons

The tracing of the resonant VUV photons is decoupled from the main computational part, the PIC/MCC simulation, described above. From the PIC/MCC simulation we obtain the positions of excitation events to the 2^1P state, leading to the emission of 'primary' VUV photons. This state decays by emitting radiation around the central wavelength of $\lambda_0 = 58.4334$ nm to the He ground state. The spectral line is broadened due to the finite lifetime (being 0.56 ns [43]) of the excited state (natural broadening), due to perturbations of the emitting atom by neighboring atoms (pressure broadening) and due to the Doppler effect that causes a shift of the wavelength because of the movement of the emitters. The natural and pressure broadening establish a Lorentz profile, whereas the Doppler broadening results in a Gaussian line shape. The overall result of all these effects is a Voigt profile [44].

The propagation of the VUV photons is limited by their absorption in the gas, a process that is already appreciable at the pressures considered here. Due to the high photoabsorption cross section, the free path of the photons is much smaller than the characteristic scales of the plasma source. Following the absorption events, emission events follow, where new photons appear with a wavelength defined by the line broadening mechanism mentioned above. These absorption/emission processes repeat until eventually the photons reach one of the limiting surfaces.

As an alternative of describing these processes by spectral distributions, VUV photons can also be treated as individual particles with Monte Carlo simulation, as proposed in [45]. Here, we follow this approach, of which the detailed description can be found in [45, 46]. We deal with the resonance radiation originating from the 2^1P state only and disregard contributions to the VUV spectrum from higher ^{1}P states (in accordance with the findings of [45]). In case of a single photon, the emission wavelength is assigned randomly [45] as:

$$\lambda_1 = \tan[(R_{01} - 0.5)\pi]\Delta\lambda_L + \lambda_0, \tag{4}$$

where $\Delta\lambda_L$ represents the total homogeneous (natural + pressure) broadening [46] and R_{01} is a random number uniformly distributed over the $(0, 1)$ interval. The wavelength assigned this way to a photon is modified by the Doppler shift that is caused by the thermal motion of the radiating atom. In this procedure, firstly, a random velocity vector, $\mathbf{v}_A$, for the (radiating) atom is sampled from the Maxwell–Boltzmann distribution of the background atoms. Secondly, a random direction, via a unit vector $\hat{\mathbf{e}}_{ph}$, to the radiated photon is assigned. With these quantities the photon is radiated with a wavelength [45]:

$$\lambda = \frac{(c + \hat{\mathbf{e}}_{ph} \cdot \mathbf{v}_A)}{c}\lambda_1. \tag{5}$$

The probability of the absorption of the photons in the background gas having a density n_0 during a time step Δt_{ph} is computed using

$$P = 1 - \exp(-\nu_{phabs}\Delta t_{ph}) = 1 - \exp(-n_0\sigma_{phabs}c\Delta t_{ph}), \tag{6}$$

where c is the speed of light and σ_{phabs} is the photoabsorption cross section:

$$\sigma_{\text{phabs}} = \frac{g_2}{g_1}\frac{\lambda_0^4 A_{21}}{8\pi c} V(\lambda^*), \tag{7}$$

where g_1 and g_2 are the statistical weights of the respective levels, A_{21} is the Einstein coefficient, and V is the Voigt-profile function [47]. The cross section (7) and probability of absorption during a given time step is computed by taking a randomly chosen (potentially absorbing) atom from the background gas with velocity $\mathbf{v}_{\text{B}}$, and using the wavelength

$$\lambda^* = \frac{(c - \hat{\mathbf{e}}_{\text{ph}} \cdot \mathbf{v}_{\text{B}})}{c}\lambda, \tag{8}$$

that takes into account the Doppler shift caused by the motion of the potentially absorbing atom.

As mentioned above, the positions of the events populating the 2^1P state are taken from the PIC/MCC simulations. These data contain the positions of 3×10^6 primary VUV photon emission events for each set of conditions studied. Each of the photons created this way is traced from its starting position, through its propagation, multiple absorptions and re-emissions, and finally its absorption at a part of the surrounding surfaces: the (flat) powered electrode, and the various parts of the bottom electrode.

4. Results and discussion

4.1. Spatio-temporal electron dynamics

We start the presentation of the results by displaying experimental PROES images recorded at eight specific times within the RF period, $t_i = i\ (T/8)$ with $(i = 0 \ldots 7)$. These experimental images are shown in figure 3 for the lowest pressure of 40 Pa (1st column) and the highest pressure of 140 Pa (3rd column). The 2nd and 4th columns of the same figure show the corresponding computational results. The sequence of the plots within one column corresponds to the different times within one period ($T = f^{-1}$) of the RF excitation with a cosine voltage waveform. As this voltage is applied to the top electrode, at $t = 0$ (i.e. $i = 0$, first row of figure 3, the applied voltage has a positive extremum and the RF sheath is fully expanded at the lower (structured) electrode, while the sheath is collapsed at the upper electrode.

The measurements reveal that at 40 Pa (panel (a1)) the excitation hardly penetrates into the trench, while a very intense penetration of the excitation into the trench is seen in the case of the higher pressure of 140 Pa (panel (c1)). The maximum intensity observed there is about 2–3 times higher compared to that observed near the flat part of the bottom electrode (at $y = 1$ cm) at the same time, or that observed near the top electrode half a RF period later. This indicates that at high pressure excitation is strongly confined to the trench region at the expansion phase of the adjacent sheath. The presence of the trench has, however, an effect on the spatial distribution of the excitation rate even in the lower-pressure case: the highest excitation rate (being about twice the rate at positions far from the trench) occurs right above the trench, indicating that the electrons emitted from the bottom and the side walls of the trench due to ion bombardment get accelerated and multiplied even though these cannot create excitation within the trench (panel (a1)).

The efficient excitation and ionization within the trench at some specific conditions (at higher pressures) originates from the hollow cathode effect [48–51], which can establish in both DC and RF plasma sources. In DC discharges, this effect may become important when surface elements of the cathode face each other (i.e., in the case of plane-parallel cathodes or a cathode with a cylindrical shape) where electrons emitted from the cathode and accelerated within the sheath adjacent to one of these elements can enter the sheath at another element. Ionization by such electrons within the sheath regions can largely enhance the ionization rate. In RF discharges, the time dependent dynamics can further increase ionization as the electron beams launched at times of sheath expansion at the various parts of the temporary cathode can interfere constructively. The strong ionization observed in the trench of the bottom electrode in our plasma sources indeed originates from the behavior.

At the next time instance ($t/T = 1/8$, panels (a2) and (c2)), the emission in the bulk becomes slightly more spread spatially at 40 Pa, as the sheath at the upper electrode starts to form and launches electrons towards the center of the plasma. At 140 Pa, excitation near the top electrode, due to the same reason shows up as well, however, this emission is confined within a narrow spatial domain, around $y = 3.5$ cm. At $t/T = 2/8$ (panels (a3) and (c3)), the excitation rate gets more confined near the top electrode, especially at the higher pressure of 140 Pa. The sheath is widest at the top electrode at $t/T = 4/8$, at the time of the negative peak of the applied voltage waveform (panels (a5) and (c5)). Interestingly, excitation within the trench is also observed at this moment at 140 Pa. This is explained by the penetration of the potential into the trench, creating a significant potential at the centre of the opening of the trench even upon sheath collapse at the bottom electrode (see later).

During the time period covering $t/T = 5/8$–$7/8$ the sheath collapses at the top electrode and expands at the bottom electrode. Correspondingly, excitation at the top electrode diminishes, while near the bottom electrode, and especially within the trench amplifies (see panels (a6-8) and (c6-8) of figure 3).

The penetration of the potential into the trench plays a crucial role in forming the excitation patterns. Figure 4 displays the simulated spatio-temporal distribution of the potential, $\phi(x, y)$, for times of maximum sheath expansion at the bottom electrode ($t/T = 0/8$, panels (a1) and (b1)) and at the top electrode ($t/T = 4/8$, panels (a2) and (b2)), for 40 Pa and 140 Pa. At $t/T = 0/8$, the very high excitation rate at 140 Pa (see figure 3(d1)) is explained by the complete penetration of the potential into the trench: as it can be seen in figure 4(b1) the sheath follows closely the perimeter of the structured electrode as revealed by the equipotential lines. Upon sheath expansion the electrons are accelerated away from both vertical side walls of the trench as well as from the bottom part of the trench [33], thereby creating strong excitation by the confined high energy electrons. At lower pressure, $p = 40$ Pa, although the

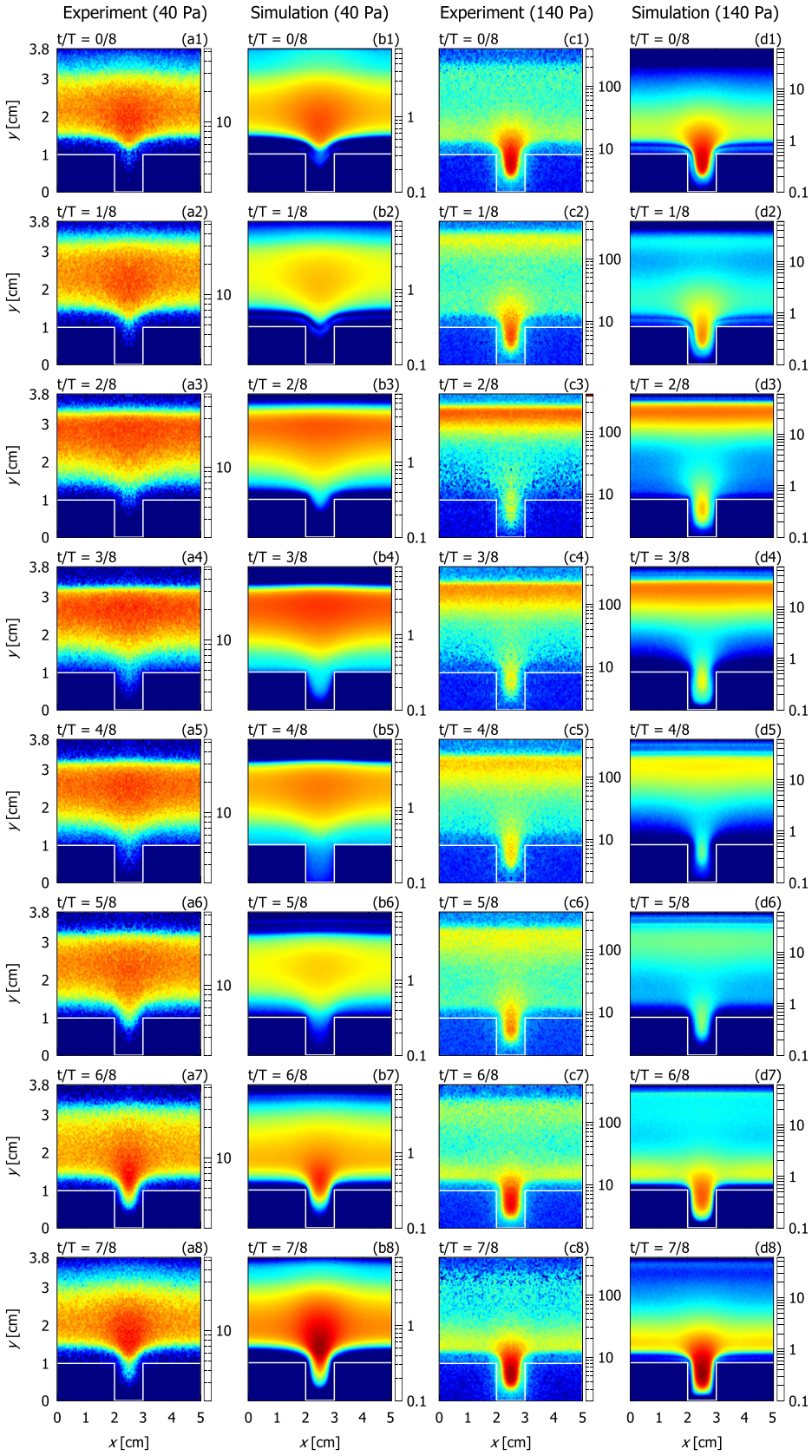

Figure 3. Time evolution of the He 3s 706 nm excitation rate obtained from the experiments (in arbitrary units) and corresponding simulation results (in units of 10^{15} cm^{-3} s^{-1}) for 40 Pa (1st and 2nd columns) and for 140 Pa (3rd and 4th columns). The bottom part of the grounded (structured) electrode (of which the contour is marked by the white lines) is situated at $y = 0$ cm, while the powered electrode is at $y = 3.8$ cm.

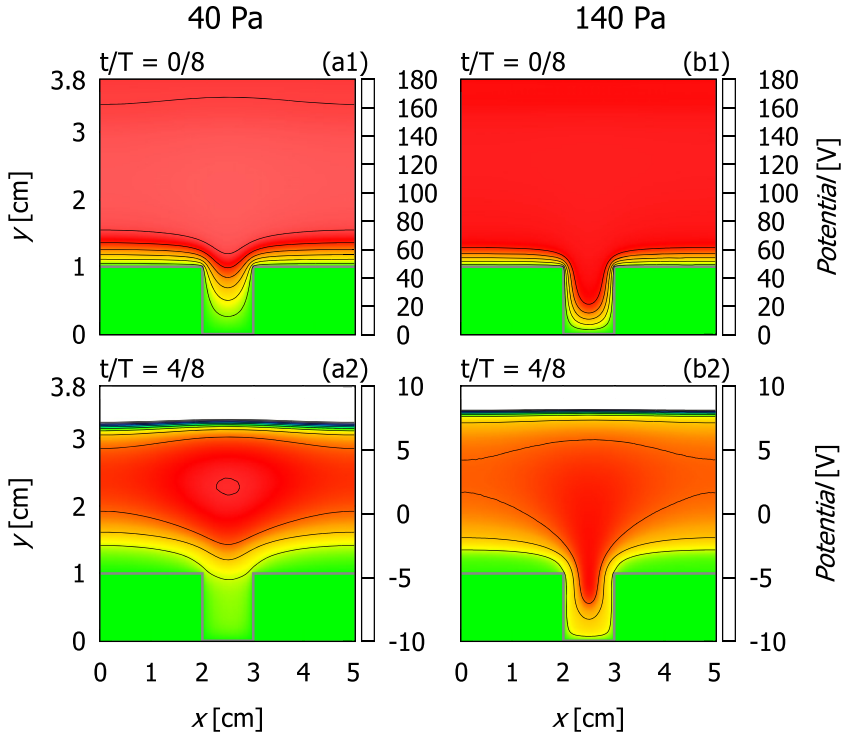

Figure 4. Computed electric potential distributions (in V) for pressures 40 Pa (left column) and 140 Pa (right column) at times $t/T = 0/8$ and $t/T = 4/8$. The potential distributions within the regions with high positive/negative values are not resolved. The (black) contour lines are separated by 25 V in the top row and by 2 V in the bottom row. The gray lines mark the edges of the bottom electrode. Note, that the potential distributions include the effect of the DC self-bias voltage, resulting in max. potentials: (a1) 156 V, (b1) 142 V ($\eta = -21.6$ V for 40 Pa), (a2) 8.0 V, and (b2) 7.3 V ($\eta = -33.1$ V for 140 Pa).

equipotential lines indicate only a moderate penetration of the potential into the trench, the potential at the centre of the opening of the trench is still about 125 V, which accelerates electrons out of the trench towards the centre of the plasma. This is why, although bright emission is not observed inside the trench, the strongest excitation occurs right above the trench (see figure 3(b1)). The effect is even stronger at the time of sheath expansion; figure 3(b8).

Excitation observed within the trench at sheath collapse, especially at the higher pressure (140 Pa) (see figure 3(d5)) is also explained by the specific potential distribution at this time instance. Figure 4(b2) shows that for this case a potential difference of ≈7 V is present between the grounded surface of the bottom electrode and the centre of the opening of the trench. This potential difference is enough to accelerate some electrons to the excitation threshold. At the lower pressure of 40 Pa, the penetration of the potential into the trench is marginal and, correspondingly, a very weak excitation is observed in the PROES maps.

The computational results corresponding to the experimental conditions are plotted in the 2nd and 4th columns of figure 3, respectively, for $p = 40$ Pa and 140 Pa. The numerical results largely corroborate the experimental observations. The sheath expansion and collapse phases can clearly be identified and excitation in the trench region is also observed at all times. As a small difference one can point out that the faintest emission from this region is seen at $t/T = 2/8$–$3/8$ in the experiment, while this occurs somewhat later, at $t/T = 4/8$ in the simulation results. The positions of the maxima of the excitation rate show a very good agreement. Weak excitation within the trench upon sheath collapse, is also seen in the simulation data, as in the case of experiments.

Spatio-temporal distributions of the excitation rate, $S_{\mathrm{exc}}(y, t)$, in two regions of the discharge, i.e., in its 'central' part, coalescing with the position of the trench (2.25 cm $\leqslant x \leqslant$ 2.75 cm), and in the 'outer' part, being far from the trench (0 cm $\leqslant x \leqslant$ 1 cm and 4 cm $\leqslant x \leqslant$ 5 cm) are presented in figure 5. These regions have been defined in figure 2(b) as region A and region B, respectively. The first pair of columns of figure 5 shows the experimental data and simulation results for region A. The corresponding data for region B are displayed in the second pair of columns.

The experimental and simulation results are generally in a very good agreement again, although the measured excitation patterns are somewhat more extended in time. The most intensive excitation occurs always near the edge of the expanding sheath, corresponding to the α-mode of discharge operation [52]. Interestingly, we observe a significant disparity between excitation peaks in the vicinity of the two electrodes. In region A (i.e. at the position of the trench), excitation near the bottom electrode is always more intensive than that near the top electrode. In region B, the situation is reversed: excitation near the top electrode is stronger than that near the bottom electrode.

In region A, the peak of excitation shows up at low pressure above the trench ($y \geqslant 1$ cm), while with increasing pressure this peak moves inside the trench ($y \leqslant 1$ cm). In this case

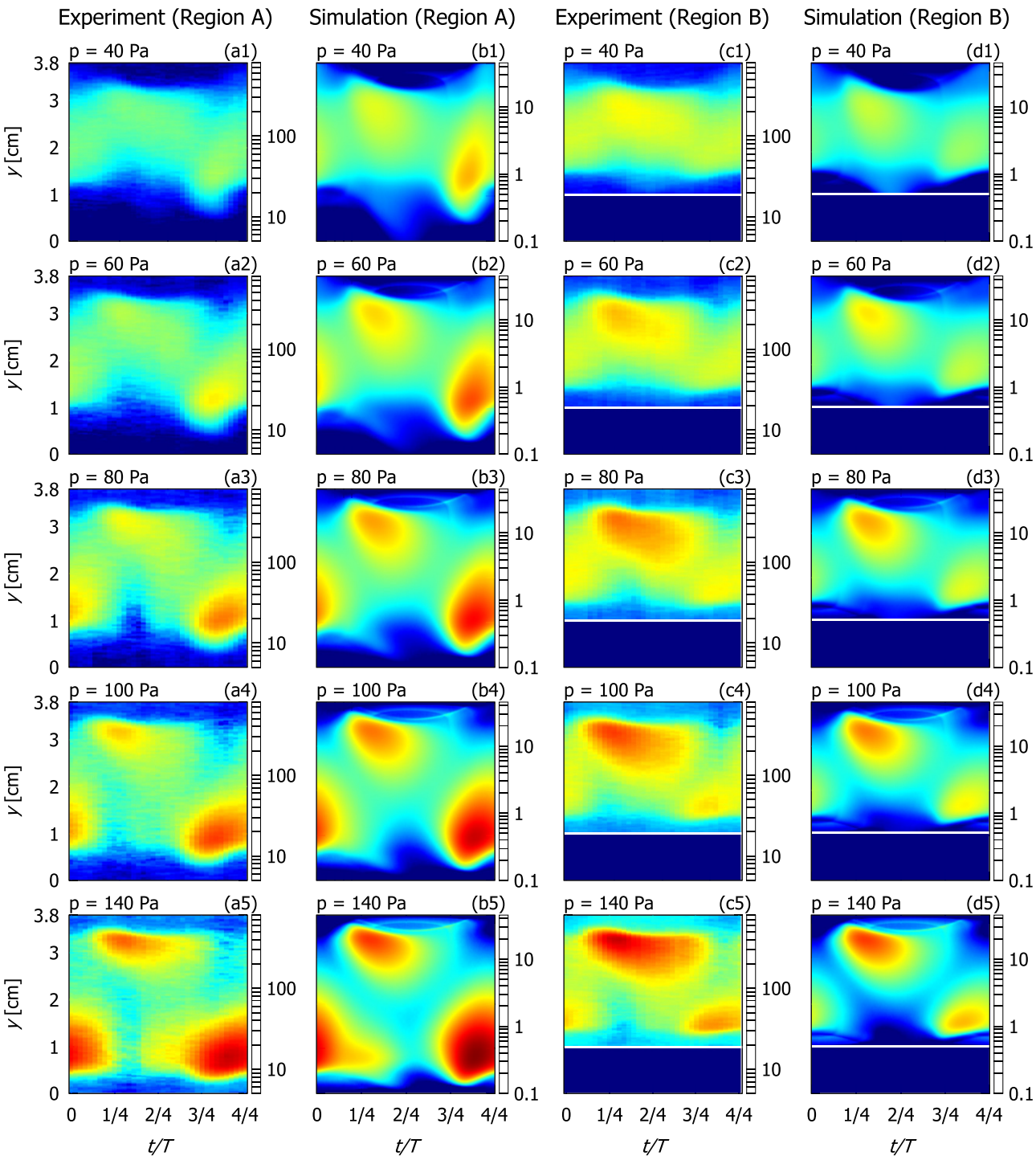

Figure 5. Spatio-temporal distributions of the excitation rate of the He 706 nm line in regions A ('central' part of the discharge around the middle of the trench, 1st and 3rd columns) and B ('outer' part of the discharge, far from the trench, 2nd and 4th columns), at various pressures (rows). For the identification of these regions see also figure 2(b). The first two columns show the data for 40 Pa, while the second pair of columns for 140 Pa. The experimental results are given in arbitrary units, while the simulation results are given in units of 10^{15} cm^{-3} s^{-1}. The bottom part of the grounded (structured) electrode is situated at $y = 0$ cm, while the powered electrode is at $y = 3.8$ cm.

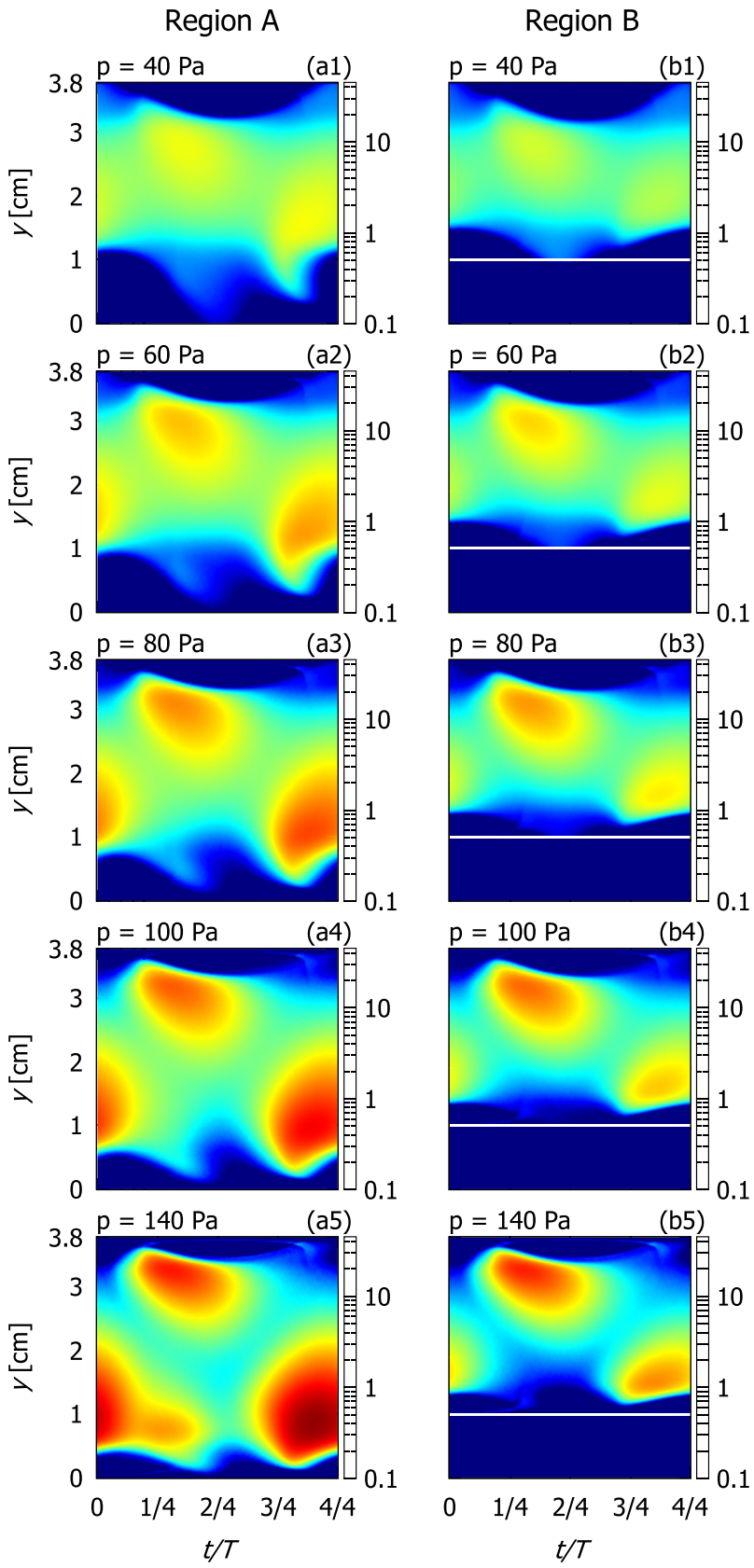

Figure 6. Spatio-temporal distributions of the He ionization rate computed in regions A ('central' part of the discharge around the middle of the trench, 1st column) and B ('outer' part of the discharge, far from the trench, 2nd column), at various pressures (rows). For the identification of these regions see also figure 2(b). The data are given in units of 10^{15} cm^{-3} s^{-1}. The bottom of the grounded (structured) electrode is situated at $y = 0$ cm, while the powered electrode is at $y = 3.8$ cm. The white line marks the top edge of the grounded electrode.

(e.g., at 140 Pa, panels (a5) and (b5)) the excitation is very intense, as the expansion of the sheath from the bottom part of the trench and from its sidewalls interfere constructively, which results in a pronounced acceleration of the electrons [33]. Excitation near the powered (top) electrode gets also more intensive at higher pressure but excitation near the trench orifice dominates strongly.

The analysis of the excitation rate in region B (see columns 3 and 4 of figure 5) reveals that, excitation near the top electrode is stronger at all conditions. Its intensity increases with increasing pressure, while its position moves closer to the top electrode due to the decrease of the sheath length with increasing p.

In the maps of the computed distributions of the excitation rate one can observe for some conditions faint features within the sheath regions. These features originate from fast electrons that enter the sheath from the direction of the other electrode, as analysed recently in [53]. These electrons can penetrate the sheath to a depth determined by their energy and the sheath potential, and at some point they turn back and leave the sheath. As both the energy of incoming electrons and the sheath potential vary with time, the sets of turning points of such electrons form specific 'intra-sheath' patterns. As the signal to noise ratio of the experimental data is worse than that of the computational results, the faint patterns are hardly visible in the experimental data. As exceptions, panels (a4) and (a5) of figure 5 can be mentioned, where some resemblance with the numerical results shown in (b4) and (b5) can be seen in the vicinity of the upper electrode.

We note that some of these structures are also visible in the spatio-temporal distributions of the ionization rate, which is shown next, in figure 6, for regions A and B, and for different pressures.

The ionization patterns also reveal a dominant α-mode operation (electron power absorption) in the discharge. The maxima of the ionization rate near the two electrodes has a disparity, similarly to the excitation rate discussed above. Signatures of the γ-mode, i.e., ionization at times of fully expanded sheath (at $t/T = 0$ at the bottom electrode and at $t/T = 1/2$ at the top electrode) by electrons emitted from the electrodes do not show up in these distributions. The reason for this lies in the relatively low discharge voltage (170 V amplitude).

4.2. Ion and photon fluxes to surfaces

The fluxes of the He^+ ions and VUV (resonant) photons at the various parts of the structured electrode are plotted in figures 7(a) and (b), respectively, as a function of pressure. The flux of the ions reaching the various segments of the structured electrode (see the sketch at the top of figure 7 for their identification) is directly obtained from the PIC/MCC simulation, while the flux of the VUV photons is determined by tracing these photons using the method described in section 3.2 (from their position of creation as obtained in the PIC/MCC simulation of the plasma to their position of absorption at the electrodes). The tracing of the photons, similarly as the tracing of the charged particles in the PIC/MCC simulation, uses periodic boundary conditions at the left/right sides of the computational domain (shown in figure 2(b)).

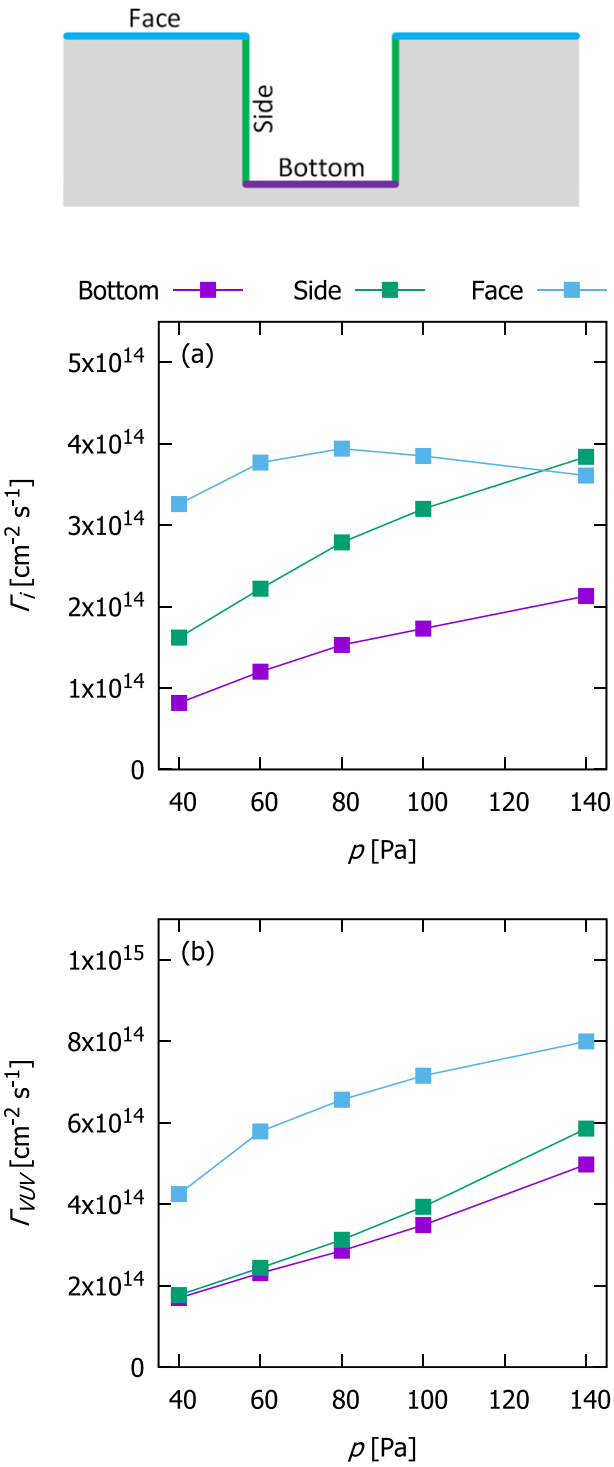

Figure 7. Pressure dependence of the helium ion flux (a) and the VUV photon flux (b) onto the individual segments of the structured electrode.

The total flux of both the ions and VUV photons increases with increasing pressure as a consequence of the enhanced charged particle density and discharge current. Among the 'partial' fluxes it is only the flux of the ions over the 'face' (flat) part of the structured electrode that exhibits a non-monotonic

behavior. This flux is maximum at 80 Pa, while the fluxes at the side walls and the bottom part of the trench increase monotonically. As at higher pressures a significant part of the excitation and ionization occurs within the trench region, the ion flux at the side wall exceeds the fluxes to the other surfaces. These effects are determined to a large extent by the relation of two characteristic length scales: the dimension of the trench and the mean free path of the electrons for inelastic processes. As an illustration, the ionization cross section of He peaks at around 100 eV energy, where $\sigma_i \approx 3.5 \times 10^{-17}$ cm^2. At 40 Pa, this results in an ionization mean free path of $\lambda_i \approx 3$ cm, while at 140 Pa, $\lambda_i \approx 0.8$ cm. This makes it clear that at higher pressures increased excitation and ionization can take place within the trench compared with lower pressures.

A similar scenario has been discussed in references [54, 55], where discharge formation in microstructure arrays was investigated at different gas pressures via 2D PIC/MCC simulations. These studies allowed to follow the penetration of the discharge into the structures and the formation of coupled micro-hollow cathode discharges with increasing pressure. At such conditions, the electron power absorption inside the cavities was found to be appreciable as revealed from the moment analysis of the electron Boltzmann equation and the EEDF exhibited an overpopulated high-energy tail. A strong connection was demonstrated to exist between the free path of the electrons and the device dimensions. Another discharge operation mode, when the discharge moves outside the microcavities, was also found in [54, 55] at further increased pressure, in our studies no attempts were made to reach conditions for this mode transition.

Regarding the fluxes of the VUV photons, we can also see a faster increase at the surface parts of the trench as compared to the 'face' of the bottom electrode. At the highest pressure the differences become insignificant, indicating that high photon fluxes can be reached inside the structures. This is true even when excitation and ionization within the trench itself is weak, even at such conditions (e.g., at 40 Pa) ion and photon fluxes in the order of 10^{14} cm^{-2} s^{-1} are predicted by the simulations. Comparing the ion and photon fluxes one may note that the ion fluxes are always much (about a factor of two) higher at the side walls of the trench as compared to the bottom part, the VUV photon fluxes reaching these two parts of the electrode are very near each other for all conditions. This results from the fact that while ions follow the electric field lines, the photons are unaffected by the electric field and can have a very uniform flux over the surface domains due to the specific (trapped) transport of the radiation. This behavior points out the advantage of the sterilization based on VUV photons, in the case of objects having complicated shapes. However, it should be noted that while this is the case for the dimensions shown here, trenches with higher aspect ratios (i.e. narrower and/or deeper) are likely to suffer from shadowing effects, where VUV radiation produced in the bulk plasma may not reach the bottom of the trench.

Figure 8 shows the spectral distribution of the wavelengths of the VUV resonant photons upon their arrival at the electrodes (without distinguishing their various parts) at 140 Pa. The dip at the line centre originates from the extremely high

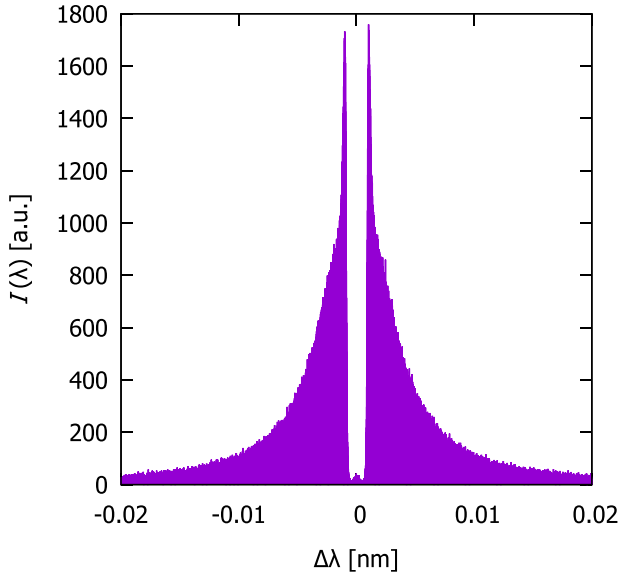

Figure 8. Distribution of the wavelength of the resonance VUV photons arriving at the electrodes (without distinguishing their various parts) at 140 Pa. $\Delta\lambda = \lambda - \lambda_0$, where λ_0 is the central wavelength of the resonant transition.

photoabsorption cross section of the radiation at that wavelength. Due to the wavelength redistribution appreciable wings of the line develop. This specific line shape does not have any consequences on the treatment of materials in such plasma sources, however, the flux of the VUV photons reaching specific parts of the electrodes is influenced by the characteristics of their propagation, which is in turn, related to the distribution of the wavelengths. Among the line broadening mechanisms mentioned in section 3.2 the Doppler broadening is found to play the dominant role.

More information about the ions reaching the surfaces is provided by their time-averaged energy distributions computed at the different segments of the structured electrode, see figure 9. Ion energy distributions at the electrodes depend generally (i) on the collisionality of the sheath, i.e., on the ratio of the sheath length and the mean free path of the ions, and (ii) on the relation between the ion transit time via the sheath and the period of the RF excitation. As revealed from figure 3, the maximum sheath length is $s \approx 0.5$ cm for 40 Pa and $s \approx 0.15$ mm for 140 Pa. At 50 eV energy, e.g., the total collision cross section of He^+ ions is $\sigma_+ \approx 1.6 \times 10^{-15}$ cm^2. At 40 Pa and 140 Pa, respectively, their free path is thus $\lambda_+ \approx 0.06$ cm and 0.019 cm, which are significantly smaller than the respective values of the sheath length. Under these conditions the ion transport through the sheath is collisional, which is in turn confirmed by the dominance of low-energy ions in the distributions shown in figure 9. The peaks in the distributions are caused by the collisions of the ions within the sheath [56, 57]. Disregarding the DC self-bias, the mean sheath voltage is about half of the amplitude of the RF voltage, being 85 V. The ion energy spectrum shows a cutoff near this energy for all conditions. (Because of the poor signal to noise ratio around this energy, the high-energy part of the distributions is not shown in figure 9.) The mean energy values of the

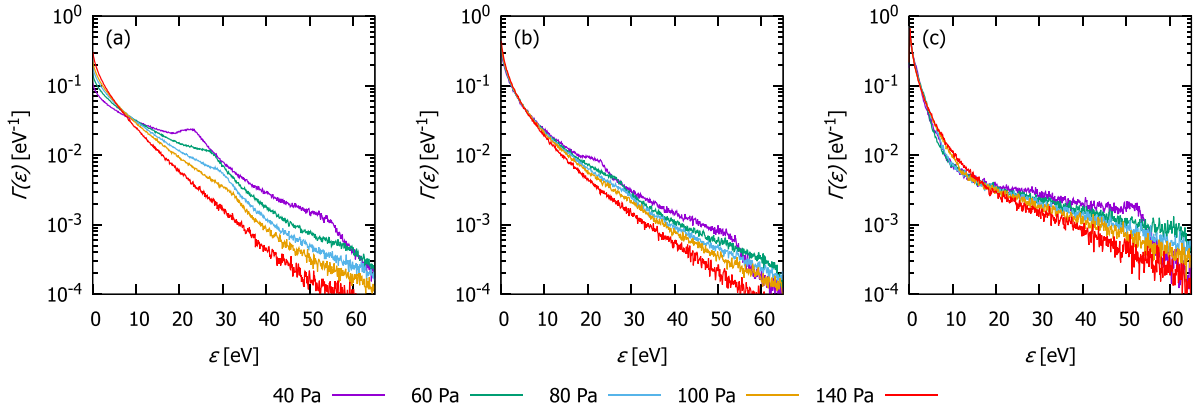

Figure 9. Energy distribution functions of helium ions colliding with (a) the 'face' segment, (b) the 'side' segment and the (c) 'bottom' segment of the trench of the structured electrode.

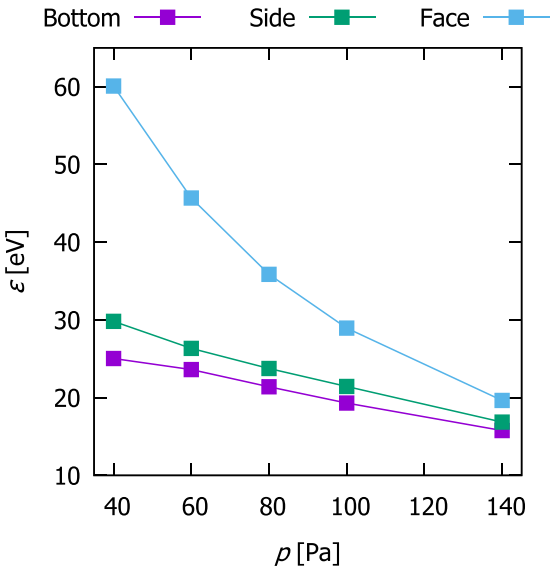

Figure 10. Evolution of the mean kinetic energy of helium ions reaching the different segments of the structured electrode as a function of the pressure.

ions reaching the various surface elements of the structured electrode are shown in figure 10. These data reveal that the mean energy drops considerably at the 'face' of the electrode only, roughly as $\langle\varepsilon\rangle \propto p^{-1}$. At the side and bottom segments, however, this decay appears to be closer to linear.

4.3. Application-relevant insights

This study has focused on understanding the charged particle dynamics and fluxes incident on surfaces in a well-defined two-dimensional model system. In application-relevant scenarios, such as the sterilisation or deposition of coatings on medical implants, more complex gas mixtures and surface structures may be present. While these complexities will lead to quantitatively different results, some general application-relevant conclusions can be drawn from the results of this work that should be relevant for surface structures with similar dimensions (≈1 cm).

Firstly, as has been demonstrated in previous studies, the presence of a structured electrode has a strong influence on the electron dynamics in the plasma [15, 58, 59]. This effect is also found to be strongly dependent on the gas pressure over the pressure range studied. As a result, variation of the pressure in this range represents an effective method to control the electron dynamics, that could be exploited to enable enhanced dissociation of molecules close to surfaces, for example.

With respect to ion and photon fluxes, PIC/MCC simulations have predicted that these are also significantly influenced by the operating pressure within the studied range. The absolute fluxes of He^+ ions and VUV photons at 58 nm are in a similar range. In addition, while the fluxes of ions and photons were generally found to be higher for the 'face' part of the electrode for most conditions, significant fluxes of these species could still be delivered to both the bottom and side walls of the trench in all cases. In the case of ions, the relationship between fluxes to the three different surfaces was found to be relatively complex with changing pressure, likely due to variation in the complex electric field structure within the trench. For photons, similar fluxes were found at both the bottom and side walls of the trench due to the isotropic distribution of photon emission, and the relatively low aspect ratio of the trench structure. For applications where UV/VUV photons are important, such as sterilisation, it can be concluded that trench structures, and potentially other structures with similar dimensions and aspect ratio, could be sterilised without significant additional effort compared to flat surfaces. Typically, the VUV fluxes measured here were about a factor 2 lower inside the trench than on the 'face' part of the electrode. In practice this would lead to a factor of two longer sterilisation time to ensure that the trench is effectively sterilised, compared to a comparable case where only the flat surface is used.

Lastly, the mean energies of positive ions incident on all surfaces was found to decrease significantly with increasing pressure, as is generally expected due to the increased rate of collisional energy transfer from ions to neutral particles. However, the decrease of mean ion energy with increasing pressure is more pronounced for the flat surface above the trench than for the surfaces within the trench. For applications where ion energy has a strong effect on the process outcome, for example,

coating deposition, it can be expected that changes in pressure would result in a divergence between coating properties above and inside the trenches due to the differing ion energy trends in each region. Given that the outcomes of material processing applications are often non-linearly dependent on the ion energy, such changes may be significant. As a result, for applications where uniform coatings are required on the surfaces of complex structures, higher pressures, where the difference between ion energies in each location is lowest, may be preferable.

5. Conclusion

A radio-frequency discharge equipped with a structured electrode, operated in helium gas at $f = 13.56$ MHz, at a peak-to-peak driving voltage of $\phi_{pp} = 340$ V was investigated experimentally and via kinetic simulations in the $p = 40$ Pa…140 Pa pressure range. 1 cm × 1 cm trenches have been machined into one of the electrodes of the experimental system. In the simulations, only one of these trenches was included with periodic boundary conditions.

The main experimental diagnostic has been PROES, while the simulations have been based on the particle in cell/Monte Carlo collisions approach, implemented in a novel GPU-accelerated code in 2D Cartesian space. The PROES measurements have been conducted on the He-I 706 nm line and have revealed the 2D temporal dynamics of the excitation rate that is intimately connected to the dynamics of the high-energy electrons in the discharge. The excitation rates computed from the PIC/MCC code were found to be in a very good agreement with the experimental data.

With an increasing pressure, an enhanced excitation was found within the trench and near its orifice, due to the constructive effect of the sheath expansion at the sidewalls and the bottom part of the trench, as revealed by monitoring the penetration of the potential into the trench. Even at low pressures, where no strong excitation within the trench was seen, the most intensive excitation occurred at/near the orifice of the trench.

While excitation and ionization within the trench was found to be prominent at the highest pressures only, a significant flux of the He^+ ions and VUV resonant photons was found at the surface elements of the trench, for all conditions. Typical values of these fluxes have been in the range of 10^{14} cm^{-2} s^{-1}. The mean energy of these ions was found to be couple of 10 eV s.

Continuation of the present studies is planned with discharges having electrodes with more complicated structures. VUV photons, in particular, are expected to play a major role under such conditions as their transport is not influenced by the electric field and this way they can reach elements of the target that are shielded from the ions.

Acknowledgments

This work was partially supported by the Hungarian Office for Research, Development and Innovation (NKFIH) Grant K134462, the Slovak Research and Development Agency under Project Nr. APVV-19-0386 and the Comenius University Grant UK/205/2021. We thank I Korolov for sharing the acquisition program of the PROES data and B Hartmann for contributions to the data acquisition system.

Data availability statement

The data that support the findings of this study are available upon reasonable request from the authors.

ORCID iDs

Ján Ďurian https://orcid.org/0000-0002-3351-6279
Peter Hartmann https://orcid.org/0000-0003-3572-1310
Štefan Matejčík https://orcid.org/0000-0001-7238-5964
Andrew R Gibson https://orcid.org/0000-0002-1082-4359
Zoltán Donkó https://orcid.org/0000-0003-1369-6150

References

[1] Samukawa S *et al* 2012 *J. Phys. D: Appl. Phys.* **45** 253001
[2] Santos M, Bilek M M M and Wise S G 2015 *Biosurface Biotribol.* **1** 146–60
[3] Moisan M, Barbeau J, Moreau S, Pelletier J, Tabrizian M and Yahia L H 2001 *Int. J. Pharm.* **226** 1–21
[4] Lerouge S, Wertheimer M R and Yahia L H 2001 *Plasmas Polym.* **6** 175–88
[5] Fiebrandt M, Lackmann J-W and Stapelmann K 2018 *Plasma Process Polym.* **15** 1800139
[6] Gans T, Schulz-von der Gathen V and Döbele H F 2004 *Contrib. Plasma Phys.* **44** 523–8
[7] Nemschokmichal S, Dittmann K and Meichsner J 2008 *IEEE Trans. Plasma Sci.* **36** 1360–1
[8] Dittmann K, Matyash K, Nemschokmichal S, Meichsner J and Schneider R 2010 *Contrib. Plasma Phys.* **50** 942–53
[9] Schulze J, Schüngel E, Donkó Z, Luggenhölscher D and Czarnetzki U 2010 *J. Phys. D: Appl. Phys.* **43** 124016
[10] Melzer A, Hübner S, Lewerentz L, Matyash K, Schneider R and Ikkurthi R 2011 *Phys. Rev.* E **83** 036411
[11] Schmidt H, Sansonnens L, Howling A A, Hollenstein C, Elyaakoubi M and Schmitt J P 2004 *J. Appl. Phys.* **95** 4559
[12] Lee H S, Lee Y S, Seo S H and Chang H Y 2010 *Appl. Phys. Lett.* **97** 081503
[13] Lee H S, Lee Y S, Seo S H and Chang H Y 2011 The characteristics of the multi-hole RF capacitively coupled plasma discharged with neon, argon and krypton *Thin Solid Films* **519** 6955–9
[14] Geyter N D, Morent R, Vlierberghe S V, Frère-Trentesaux M, Dubruel P and Payen E 2011 *Prog. Org. Coat.* **70** 293–9
[15] Wang L, Hartmann P, Donkó Z, Song Y H and Schulze J 2021 *J. Vac. Sci. Technol.* A **39** 032202
[16] Horváth B, Derzsi A, Schulze J, Korolov I, Hartmann P and Donkó Z 2020 *Plasma Sources Sci. Technol.* **29** 055002
[17] Wiese W L and Fuhr J R 2009 *J. Phys. Chem. Ref. Data* **38** 565–720
[18] Birdsall C and Langdon A 2004 *Plasma Physics via Computer Simulation* (*Series in Plasma Physics and Fluid Dynamics*) (London: Taylor and Francis)

[19] Verboncoeur J P 2005 *Plasma Phys. Control. Fusion* **47** A231–60

[20] Matyash K, Schneider R, Taccogna F, Hatayama A, Longo S, Capitelli M, Tskhakaya D and Bronold F X 2007 *Contrib. Plasma Phys.* **47** 595–634

[21] Tskhakaya D, Matyash K, Schneider R and Taccogna F 2007 *Contrib. Plasma Phys.* **47** 563–94

[22] Sun A, Becker M M and Loffhagen D 2018 *Plasma Sources Sci. Technol.* **27** 054002

[23] Horváth B, Daksha M, Korolov I, Derzsi A and Schulze J 2017 *Plasma Sources Sci. Technol.* **26** 124001

[24] Becker M M, Kählert H, Sun A, Bonitz M and Loffhagen D 2017 *Plasma Sources Sci. Technol.* **26** 044001

[25] Derzsi A, Korolov I, Schüngel E, Donkó Z and Schulze J 2015 *Plasma Sources Sci. Technol.* **24** 034002

[26] Alexandrov A L and Schweigert I V 2005 *Plasma Sources Sci. Technol.* **14** 209–18

[27] Erden E 2013 Simulation of glow discharge plasmas by using parallel particle in cell/Monte Carlo collision method: the effects of number of super particles used in the simulations http://etd.lib.metu.edu.tr/upload/12616609/index.pdf

[28] Juhasz Z, Ďurian J, Derzsi A, Matejčík Š, Donkó Z and Hartmann P 2021 *Comput. Phys. Commun.* **263** 107913

[29] Claustre J, Chaudhury B, Fubiani G, Paulin M and Boeuf J P 2013 *IEEE Trans. Plasma Sci.* **41** 391–9

[30] Shah H, Kamaria S, Markandeya R, Shah M and Chaudhury B 2018 A novel implementation of 2D3V particle-in-cell (PIC) algorithm for Kepler GPU architecture *2017 IEEE 24th Int. Conf. on High Performance Computing (HiPC)* (Jaipur, India 18–21 December 2017)

[31] Hartmann P *et al* 2020 *Plasma Sources Sci. Technol.* **29** 075014

[32] Wang L, Hartmann P, Donkó Z, Song Y-H and Schulze J 2021 *Plasma Sources Sci. Technol.* **30** 054001

[33] Wang L, Hartmann P, Donkó Z, Song Y-H and Schulze J 2021 *J. Vac. Sci. Technol.* A **39** 063004

[34] Lymberopoulos D P and Economou D J 1995 *J. Res. Natl Inst. Stand. Technol.* **100** 473

[35] Kim H C, Iza F, Yang S S, Radmilović-Radjenović M and Lee J K 2005 *J. Phys. D: Appl. Phys.* **38** R283

[36] Donkó Z, Derzsi A, Vass M, Horváth B, Wilczek S, Hartmann B and Hartmann P 2021 *Plasma Sources Sci. Technol.* **30** 095017

[37] Biagi S F 2010 *Fortran Program, MAGBOLTZ v8.92* www.lxcat.net (accessed 22 October 2021)

[38] Phelps A V 1994 *J. Appl. Phys.* **76** 747–53

[39] Phelps A V 2005 Compilation of atomic and molecular data http://jila.colorado.edu/avp/

[40] Doughty D A, Den Hartog E A and Lawler J E 1987 *Phys. Rev. Lett.* **58** 2668

[41] Den Hartog E A, Doughty D A and Lawler J E 1988 *Phys. Rev.* A **38** 2471

[42] Schulenberg D A, Korolov I, Donkó Z, Derzsi A and Schulze J 2021 *Plasma Sources Sci. Technol.* **30** 105003

[43] Itnik M, Stani A, Buar K, Lambourne J G, Penent F, Hall R I and Lablanquie P 2003 *J. Phys. B: At. Mol. Opt. Phys.* **36** 4175

[44] Kunze H J 2009 *Introduction to Plasma Spectroscopy* vol 56 (Berlin: Springer)

[45] Fierro A, Moore C, Scheiner B, Yee B T and Hopkins M M 2017 *J. Phys. D: Appl. Phys.* **50** 065202

[46] Donkó Z, Hamaguchi S and Gans T 2018 *Plasma Sources Sci. Technol.* **27** 054001

[47] McLean A B, Mitchell C E J and Swanston D M 1994 *J. Electron Spectrosc. Relat. Phenom.* **69** 125–32

[48] Little P F v E A 1954 The hollow-cathode effect and the theory of glow discharges *Proc. R. Soc.* A **224** 209–27

[49] Helm H 1972 *Z. Naturforsch.* A **27** 1417–25

[50] Kolobov V I and Tsendin L D 1995 *Plasma Sources Sci. Technol.* **4** 551

[51] Kutasi K and Donkó Z 2000 *J. Phys. D: Appl. Phys.* **33** 1061

[52] Schulze J, Donkó Z, Derzsi A, Korolov I and Schuengel E 2014 *Plasma Sources Sci. Technol.* **24** 015019

[53] Vass M, Derzsi A, Schulze J and Donkó Z 2021 *Plasma Sources Sci. Technol.* **30** 03LT04

[54] Fu Y, Zheng B, Zhang P, Fan Q H and Verboncoeur J P 2021 *J. Appl. Phys.* **129** 023302

[55] Fu Y, Wang H, Zheng B, Zhang P, Fan Q H, Wang X and Verboncoeur J P 2021 *Appl. Phys. Lett.* **118** 174101

[56] Wild C and Koidl P 1991 *J. Appl. Phys.* **69** 2909–22

[57] Schüngel E, Donkó Z and Schulze J 2017 *Plasma Process Polym.* **14** 1600117

[58] Schmidt N, Schulze J, Schüngel E and Czarnetzki U 2013 *J. Phys. D: Appl. Phys.* **46** 505202

[59] Doyle S J, Lafleur T, Gibson A R, Tian P, Kushner M J and Dedrick J 2017 *Plasma Sources Sci. Technol.* **26** 125005